Patterns of Bubble Clouds Organized by Langmuir Circulation

DAVID FARMER AND MING LI*

Institute of Ocean Sciences, Sidney, British Columbia, Canada

(Manuscript received 18 July 1994, in final form 26 October 1994)

ABSTRACT

A commonly observed property of near-surface bubble distributions is their collective organization into long rows aligned with the wind under the influence of Langmuir circulation. Time series observations with sonars having fixed orientation reveal the temporal evolution of bubble distributions as they drift through the sonar measurement path. Here this concept is extended to provide a time sequence, at 37-s intervals, of two-dimensional images generated by horizontally rotating sonars. Observations obtained during a storm in the Strait of Georgia show individual Langmuir convergence zones as they evolve above the freely drifting sonar. The resulting images are processed to generate a binary representation of the convergence zone patterns from which their orientation, length, spacing, and other properties can be extracted. Although there is some angular spreading, most convergence lines are aligned within 20° of the wind. The spacing between convergence lines reveals a wide range of scales, but the mean spacing increases slightly with wind speed. Measurement of downwind length reveals the presence of numerous short bubble clouds, possibly associated directly with wave breaking; however, there is a general trend toward a length that increases with wind speed.

A dominant characteristic at higher wind speeds is the formation of Y junctions in which three linear bubble clouds are joined together. Each branch of a Y junction was observed to be approximately 50 m. The junctions preferentially point downwind with the angle between the two side branches being approximately 30°. Although the junctions deform with time, they can be readily tracked through successive images. The existence of convergence zone junctions suggests the reconnection of counterrotating longitudinal vortices and the formation of U-shaped vortex tubes.

1. Introduction

Surface streaks or windrows consisting of floating materials are often seen to form long, narrow bands on the ocean surface parallel to the wind direction. These windrows are the surface manifestation of a subsurface circulation first identified by Langmuir (1938). Breaking waves introduce bubbles into the sea, which serve as excellent acoustic tracers of near-surface circulation, even in the absence of visible surface markers (Thorpe 1992a, Osborn et al. 1992). Here we discuss observations of bubble cloud distributions obtained with a novel type of sonar that acquires two-dimensional images of the surface. These allow unambiguous detection of certain bubble cloud properties, including the time-evolving patterns associated with Langmuir vortex amalgamation.

Sidescan sonars with fixed orientation have been used to detect linear bubble clouds formed in Langmuir convergence zones (Thorpe and Hall 1983; Smith et al. 1987; Zedel and Farmer 1991). The resulting time–range sonographs have been used to infer convergence zone spacing, which is found to have some dependence on wind speed. Bubble cloud patterns of this type have also been used to infer one-dimensional dispersion in the cross-wind direction (Thorpe and Cure 1994). A commonly observed feature in these sonographs is the apparent merging of adjacent bubble bands to form a "Y junction" pattern in the time–range image (Thorpe 1992b).

A difficulty in the use of time–range sonographs is that the interpretation is ambiguous. The structure appearing in a time–range image might be interpreted as a time evolution of a strictly two-dimensional feature (Fig. 1a), or as a simple advection through the sonar beam of a feature having a fixed geometry (Fig. 1b). Alternatively, the image might represent some combination of a time-evolving structure and its advection through the beam.

A fortuitous observation that illustrated a method for resolving the ambiguity was described by Zedel and Farmer (1991) in which the sonar beam was partially rotated by unintended instrument motion, thus sweeping out a two-dimensional image. Motivated by this result we modified an existing instrument (Vagle and Farmer 1992) to rotate each of four 1.5° beamwidth sonars in 1.8° steps such that a single quadrant

* Also affiliated: Centre for Earth and Ocean Research, University of Victoria, Victoria, British Columbia, Canada.

Corresponding author address: Dr. David M. Farmer, Institute of Ocean Sciences, P.O. Box 6000, 9860 West Saanich Rd., Sidney, BC V8L 4B2, Canada.

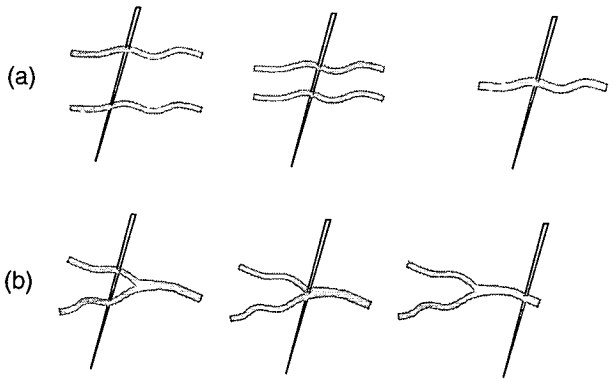

FIG. 1. Two different interpretations of bubble cloud patterns observed in time–range sonar images. In the upper interpretation (a) the convergence lines remain parallel while merging. The lower interpretation (b) shows a Y junction advected through the sonar beam.

is swept out in approximately 37 s. Provided the overall pattern does not change rapidly on this timescale, its temporal evolution can be followed in the succession of images. The resulting images can be used to derive properties of the bubble clouds, such as length, spacing, and orientation, and to make estimates of surface dispersion.

The distribution of Langmuir convergence zones changes relatively slowly so that useful tracking of their temporal evolution is possible. A requirement for the study of time-evolving patterns of convergence is that the structures not be advected beyond the imaged area before the interesting variability can be observed. In the present study advective effects were reduced by allowing the sonar to drift freely with the current.

The Y-junction convergence zone is a surface expression of the underlying vortical flows. Its existence suggests that Langmuir circulation is not fully described

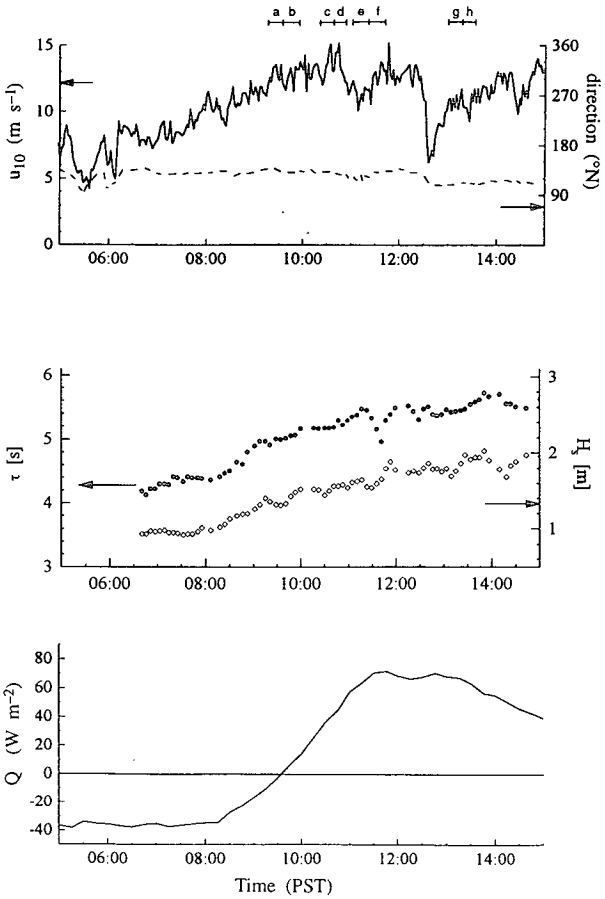

FIG. 3. Summary of meteorological data: (a) wind speed U_{10} and wind direction, (b) significant wave height and significant wave period measured with a vertical sonar, and (c) the total surface heat flux. Line segments a, b, c, etc. show times of datasets illustrated in Figs. 11–13.

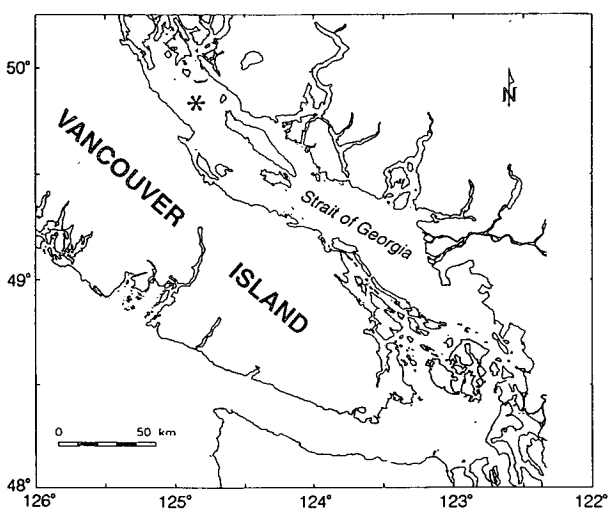

FIG. 2. Experimental site (*) in the Strait of Georgia.

as a two-dimensional pattern of parallel counterrotating vortex tubes, but may have a complex three-dimensional vortex structure, similar to the junctions found in thermal convection (Newell et al. 1993, 1990; Etling and Brown 1993), in shear flows (Thorpe 1985;

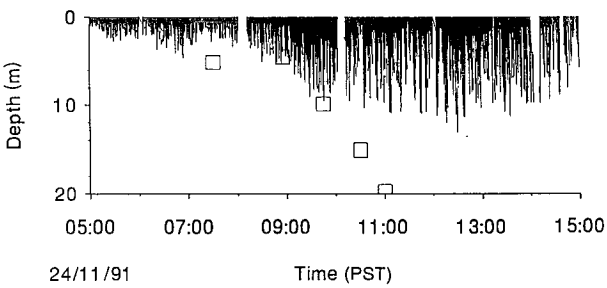

FIG. 4. Bubble cloud penetration depth determined from sonars and mixed layer depth (□). After 1100, the mixed layer deepened to 50 m.

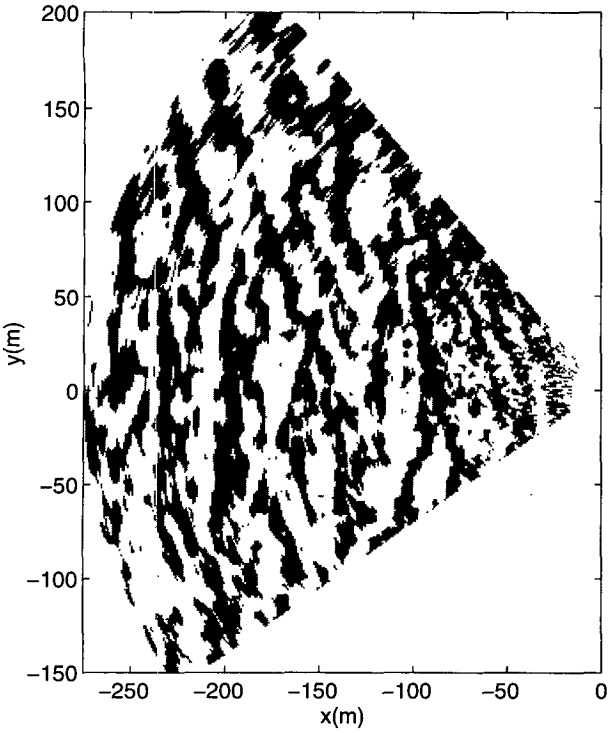

FIG. 5. A two-dimensional sonar image obtained at 1018:06 24 November 1991. To emphasize the structure, for which the dynamic range of a grayscale image is inadequate, we use a threshold below which the signal is shown as white.

Pierrehumbert and Widnall 1982) and in Gortler and Dean flows (Guo and Finlay 1994). The key mechanism common to these flows is the reconnection of counterrotating vortices (Saffman 1990; Shelley et al. 1993).

The observations discussed here were acquired in the Strait of Georgia (49°50′N, 124°48′W) over a period of 12 h during passage of a storm (24 November 1991). Some of the oceanographic and meteorological time series have previously been reported in connection with a study of air–sea gas flux (Farmer et al. 1993). Here we focus on a description of the technique including the isolation of the essential two-dimensional structures from the sonar images and the determination of resulting bubble cloud properties. A detailed three-dimensional vortex model of Langmuir circulation that provides a dynamical explanation of the processes described here forms the subject of a separate paper.

2. Experimental approach

The experiment took place in the Strait of Georgia on 24 November 1991. Figure 2 shows the deployment site. The sonar drifted at a speed of 0.16 m s^{-1} to the northwest (337° from north). Water depths were between 100 and 200 m. The wind fetch for the data reported here was 50 km.

Figure 3 summarizes the meteorological data. The wind speed increased steadily from 6 m s^{-1} at 0500 (all times LST) to 14 m s^{-1} at 1030. The wind dropped briefly between 1230 and 1300 h. The wind direction wandered before 0700 h but thereafter remained constant at 131°, until 1230 when it shifted to 116°. The significant wave height rose steadily from 1 m at 0800 to 2 m at 1300, while the wave period increased slightly from 3.7 to 4.5 s over the same period. The surface heat flux is generally small, amounting to −40 W m^{-2} heat loss before 0800, switching to 60 W m^{-2} at midday.

Figure 4 shows the time evolution of mixed layer depth determined from CTD casts and bubble penetration depth estimated from upward-looking sonars. At 0600, advection of a thin surface layer of freshwater resulted in a mixed layer depth of only 5 m. Then the

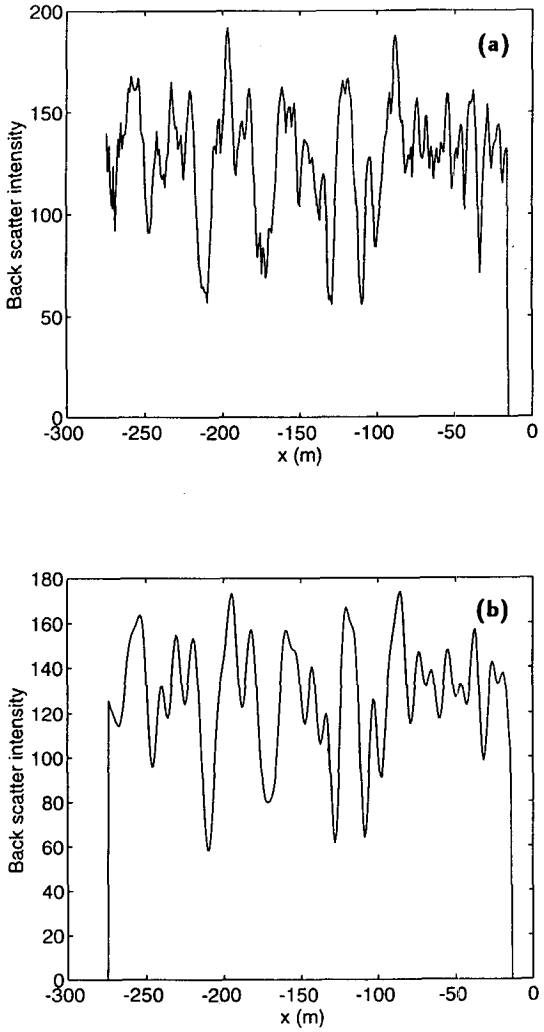

FIG. 6. Acoustic backscatter intensity measured along a line perpendicular to the wind direction for (a) unfiltered data and (b) data smoothed with elliptic filter.

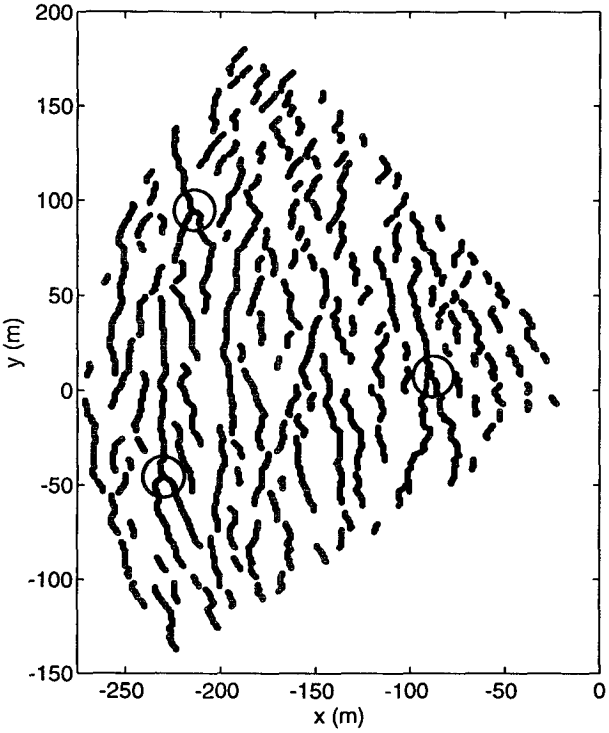

FIG. 7. Pattern of convergence lines obtained by the "ridge following" scheme. Circles identify junctions.

mixed layer deepened due to wind mixing, reaching 20 m at 1100. It continued to deepen to 50 m at 1900. Figure 4 shows that for a brief period (0900–1300) there is a close correlation between the depth of the mixed layer and the penetration depth of bubble clouds.

The sonar instrument is suspended from a surface float by a rubber cord to 24-m depth. It is therefore free to drift with the prevailing current. Four orthogonal, mechanically steered 100-kHz narrow beam sonars (1.5°) complete a scan of the sea surface in about 37 seconds. The sonar transmits a pulse of length 5 ms. In this preliminary study we were limited to the use of two sidescans. Although the figures presented here are based on signals derived from a single sonar, data from both sonars were used in the statistical measurements of bubble cloud properties.

The backscatter intensity typically varies by a factor of 100 over the useful range of measurement for each sonar transmission. The resulting azimuth and range dependent signal can be transformed into a Cartesian image using bilinear interpretation. However, we are primarily interested in a simpler representation described subsequently.

3. Identification of convergence lines in sonar images

The grayscale image displayed in Fig. 5 shows the distribution of sonar backscatter intensity in an area scanned by a single azimuthally rotating sonar beam. This image is constructed from 50 transmissions at angular steps of 1.8°. The useful range is approximately 300 m, which is divided into 1-m range bins for convenience. The actual range resolution is limited by the 5-ms pulse length, which occupies a reflected path length of 3.75 m. This resolution is not as great as can be achieved with a shorter pulse length: in this case the pulse length was dictated by the need to acquire Doppler velocity measurements. Since Langmuir circulation is relatively steady over a few tens of seconds, one can think of the sonar image as an instantaneous snapshot of the ocean surface. In Fig. 5 the sonar backscatter intensity is normalized to remove the range dependence resulting from spreading and absorption.

Bands of dark color corresponding to higher levels of backscatter intensity are easily identifiable. These bands correspond to high concentrations of bubbles that collect at the convergence lines of Langmuir circulation. This interpretation is supported by simultaneous vertical sonar images, which show the correspondence between lines of enhanced backscatter and vertical distribution of bubbles (see Zedel and Farmer 1991, Fig. 8), and in what follows we refer to these bands as convergence lines. Although these images help to visualize the patterns of bubble clouds, they are not particularly useful when we want to make quantitative measurements.

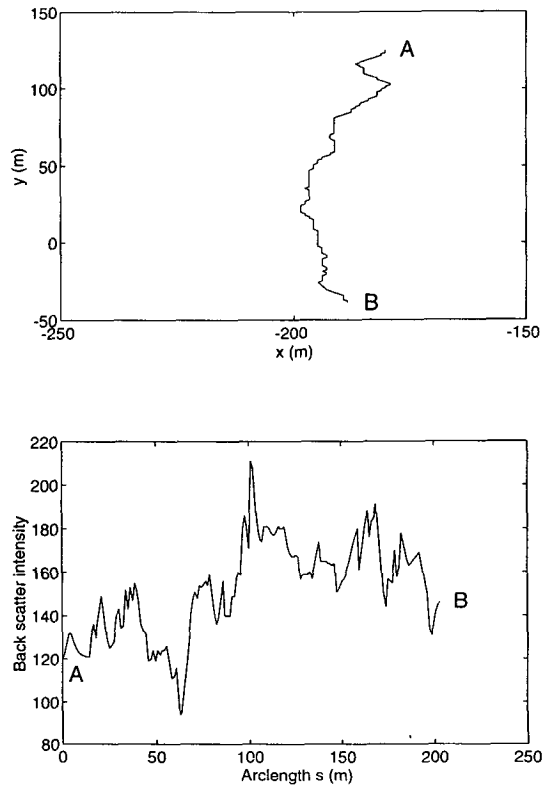

FIG. 8. An example of (a) a detected convergence line and (b) the corresponding backscatter intensity distribution along the line.

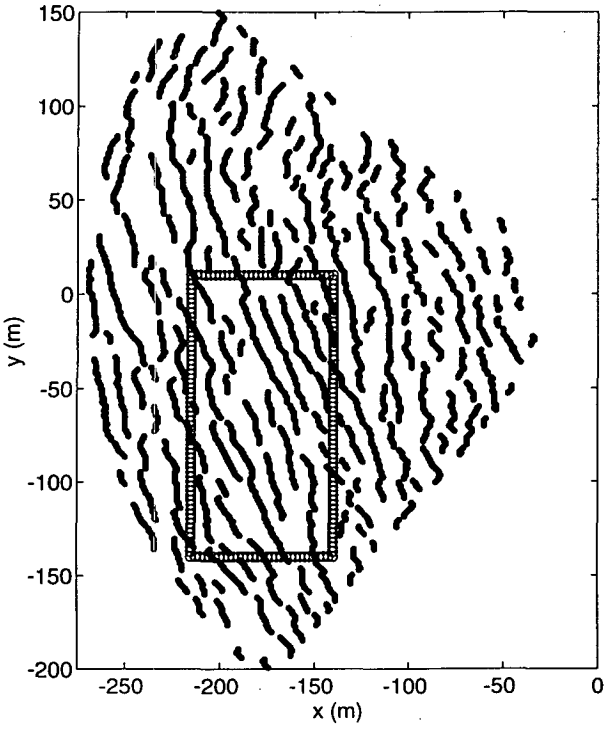

FIG. 9. A pattern of convergence lines at low wind speed (0915: 49 24 November 1991). The framed area is selected for investigation of the persistence of a convergence line, shown in Fig. 14.

To detect objectively the locations of convergence lines, we have devised a method that recognizes bands of high bubble concentration located at peak values (or local maxima) of sonar backscatter intensity. As discussed subsequently, this approach differs from a related technique developed by Thorpe and Cure (1994) for "skeletonizing" range versus time sonar images. We refer to the present method as a maxima detection scheme. Three steps are involved. First we locate sonar backscatter intensity maxima along a path perpendicular to the wind direction. Second, we connect into lines those local maxima that are closely spaced. The third step is described in section 5.

The initial sonar data are acquired in polar coordinates. These are first transformed into a 300×600 matrix in Cartesian coordinates (x, y) through a bilinear interpolation in radius and azimuth. Each row vector of the matrix is a spatial series of the sonar backscatter intensity, showing its variation along the x direction (see Fig. 6a), which is approximately orthogonal to the wind direction. The maxima of sonar intensity correspond to the locations of bubble clouds, which we identify as convergence zones of Langmuir circulation. Our task is to find the local maxima of this spatial series. Since the data contain high frequency noise, we use a low-pass elliptic filter. We have experimented with different degrees of smoothing and found that an elliptic filter of degree 4 and with cutoff distance of 5 m gives the most satisfactory result (Fig. 6b). The smoothed curve has well-defined peaks identifiable in the original data. It is these peaks, rather than the more rapid fluctuations within the peaks or valleys, that correspond to the dominant bubble cloud features. Before filtering, we subtract a mean from those elements of the spatial series that lie within the ensonified sector. This ensures that the filtered data have the same peak heights as the original data. The filter is run in both directions so as to remove phase errors. The binary representation, in terms of local backscatter maxima, depends upon relative magnitude in the area of interest rather than the actual magnitude.

Repeating this procedure for every row in the sonar intensity matrix, we obtain a collection of points in the x–y plane, as illustrated in Fig. 7. These points, obtained from the independent horizontal transects, are sufficiently closely spaced that they appear as linear features approximately aligned in the wind direction. The resulting image is fully consistent with the concept of Langmuir convergence zones oriented with the wind. Comparisons with the sonar image confirm that the lines coincide with the bands of strong backscatter (compare Figs. 5 and 7).

To extract statistical information on the properties of the resulting convergences, which thus far are only identified as linear features by visual inspection, it is necessary to use an algorithm that searches for closely spaced points and connects them numerically. We start from a local maximum and look for other maxima in its immediate neighborhood. If there is a neighboring maximum, we count the two points as being on the same line. Continuing the search, we find all points on the line. In this way, we can keep track of all convergence lines in the image.

In searching for the maximum, our low-pass filter forbids a second maximum to lie within the filter cutoff distance. Therefore, lines representing two intersecting bubble clouds do not actually meet at a point, even though the continuous image clearly indicates the presence of a junction. The third step in our algorithm, described in section 5, identifies closely spaced lines to determine the presence or absence of junctions. This step has been included in Fig. 7. We refer to this scheme, which is analogous to walking along a mountain ridge, where altitude is synonymous with acoustic backscatter intensity, as a "ridge following algorithm."

In the following analysis, we concentrate on the patterns obtained by our line detection scheme. Nevertheless it would be interesting to know how sonar backscatter intensity varies along the convergence lines. In Fig. 8 we show one example of a binary representation of a bubble cloud and its corresponding sonar intensity as a function of position along the line. The convergence line (Fig. 8a), although showing some irregularities, predominantly runs in the y direction. In Fig. 8b, the backscatter intensity is obtained from the raw data at the locations of the local maxima derived from

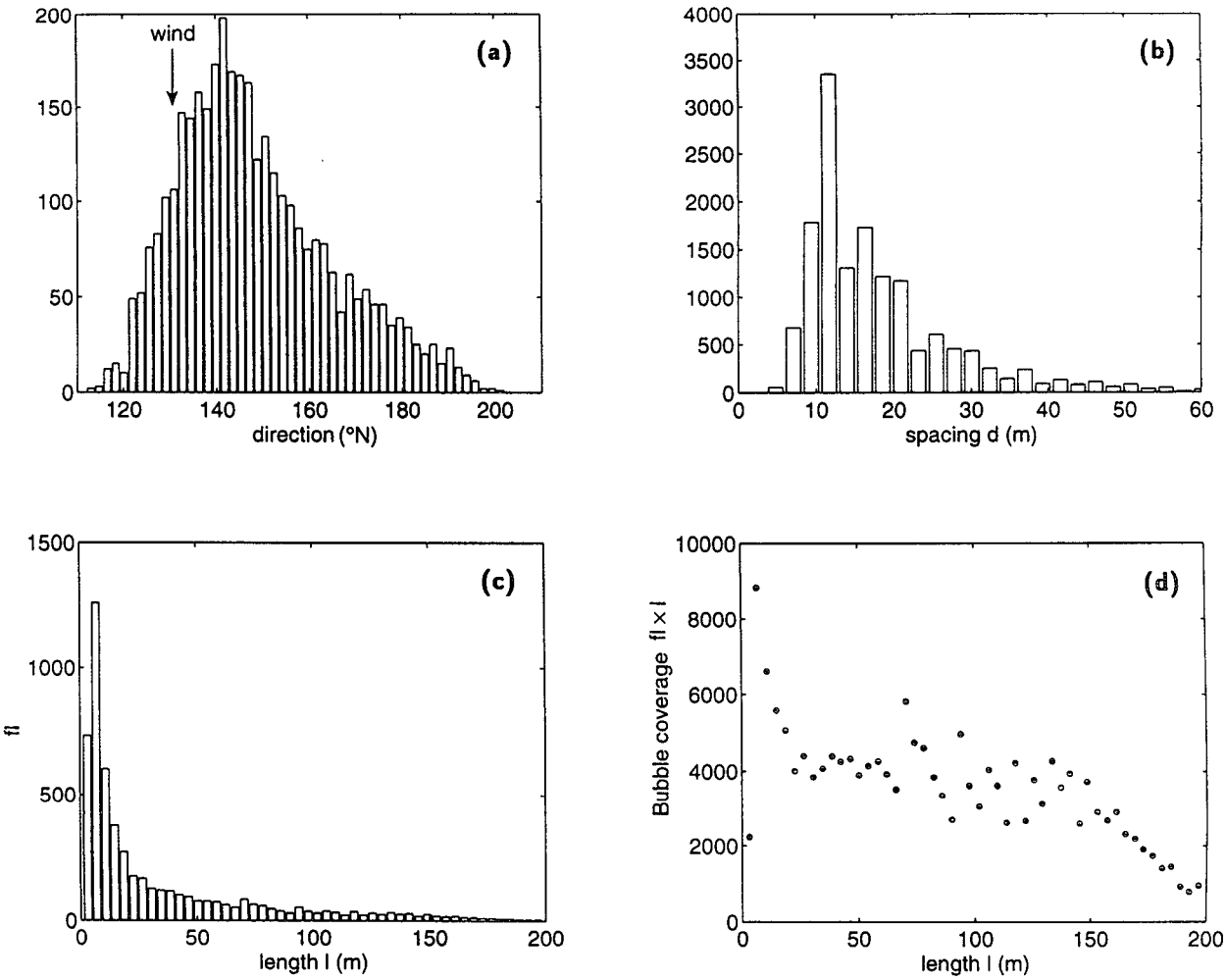

FIG. 10. Summary of measurements of convergence lines between 0915 and 0934. Histograms of (a) windrow direction, (b) spacing, (c) length, and (d) bubble coverage.

the elliptical filtering approach discussed previously. The variation of sonar intensity suggests a considerable variability of bubble concentration along the convergence line. We have calculated the autocorrelation function R_{xx} of backscatter intensity averaged over a number of long convergence lines (longer than 100 m) and found that R_{xx} drops to zero at length $l = 16$ m.

4. Measurements of convergence line properties

Once the convergence lines are mapped, we can calculate their orientation, length, spacing, and other properties. The spacing between adjacent Langmuir cells has previously been reported (e.g., Smith 1987) and visual estimates (Weller and Price 1988) have been made of orientation, but the length of coherent features cannot be unambiguously determined from fixed orientation sonars.

Although the convergence lines are somewhat irregular, we simplify the description by using a straight line least squares fit. The fit is made over the domain of the two-dimensional dataset measured in the wind direction. The direction is given by the slope and the (straight line) length by the distance between end points. For convenience these and all other calculations are carried out using a coordinate system that is approximately aligned (y axis) with the wind direction (see Figs. 5 and 7). The image, being of finite dimension, includes some convergence lines that meet the image boundary. These are not included in the subsequent statistical summary, since they will in general extend beyond the boundary and bias the results.

The spacing between adjacent windrows is derived from the locations of backscatter maxima previously calculated (see Fig. 6), using measurements at many different downwind locations. The results are corrected for small departures between the mean windrow orientation and the y axis.

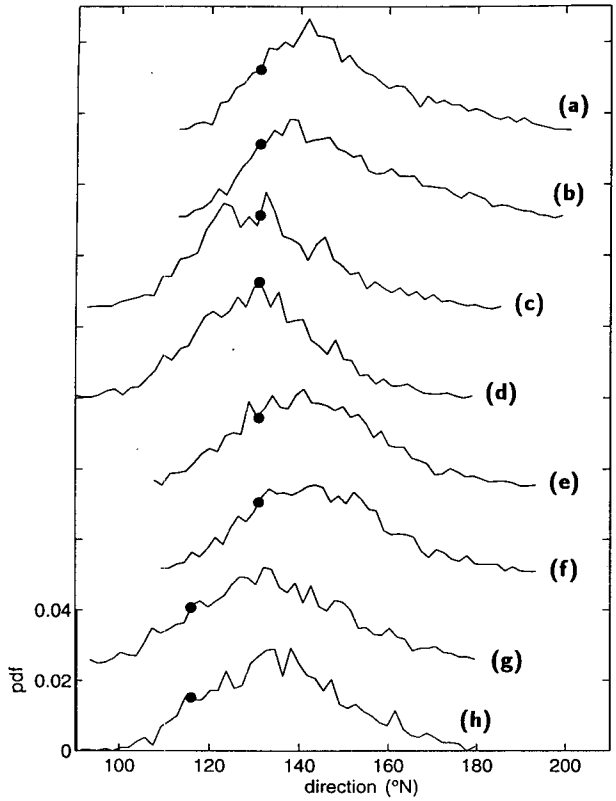

FIG. 11. Probability density function of convergence line directions, displaced successively by 0.025. The directions are not normalized. Black dots represent the wind direction during each period. (a) 0915–0934. (b) 0935–0955. (c) 1018–1035. (d) 1036–1052. (e) 1058–1118. (f) 1119–1139. (g) 1303–1320. (h) 1321–1337. (see Fig. 3).

In the following data we focus on two periods: 0915–1149 24 November, when the wind speed steadily increased, and 1300–1330, which included a large fluctuation in wind speed and a 15° shift in direction. We observed an interesting sequence of events. Convergence lines were mostly parallel at the beginning of this period, but as the wind increased, directional irregularities emerged and the convergence lines joined to form more complex patterns such as Y junctions.

Figure 9 gives an example of convergence lines at a wind speed of 10 m s^{-1} (0915), showing generally parallel features. In Fig. 10 we summarize the measurements in 30 images obtained for similar wind speeds between 0915 and 0935. The reported wind direction was 131° from north. The mean direction of convergence lines is at 148.3°, about 17° off the wind direction, but the standard deviation is only 16.6° so that most lines point in a narrow range around the mean direction (Fig. 10a). Observations during other periods show that the mean direction of convergence lines is generally in closer agreement with wind direction (see Fig. 11). These results are consistent with previous reports (Leibovich 1983) in which Langmuir circulation is found to be aligned within 15 to 20 degrees of the wind direction.

The length distribution calculated in this way, shows a large number of quite short bubble clouds (Fig. 10c). One way of looking at the relative significance of shorter bubble clouds to the total area coverage is to identify the product of length and its frequency of occurrence as a function of length. If the clouds were of uniform width, this would be equivalent to a plot of areal coverage per length increment as a function of bubble cloud length. Figure 10d shows this result, corresponding to the dataset shown in Fig. 10c. This distribution appears in virtually all of the available data to have three components: a large bubble coverage at scales < 20 m, a relatively uniform coverage for lengths between 20 and 120 m, and reduced coverage at larger scales. This suggests a different process is involved in the shorter (i.e., <20 m) bubble clouds.

We propose that the smaller bubble clouds are due to breaking waves. The dominant wave period is about 4 s, corresponding to a wavelength of 25 m. If the typical breaker wave period is 0.7 of the dominant wave period, as found by Ding and Farmer (1994), and the breaker length is 0.7 of the corresponding breaking wavelength, then we expect breaking surface waves to generate local clouds of length 0.7×0.7 of the domi-

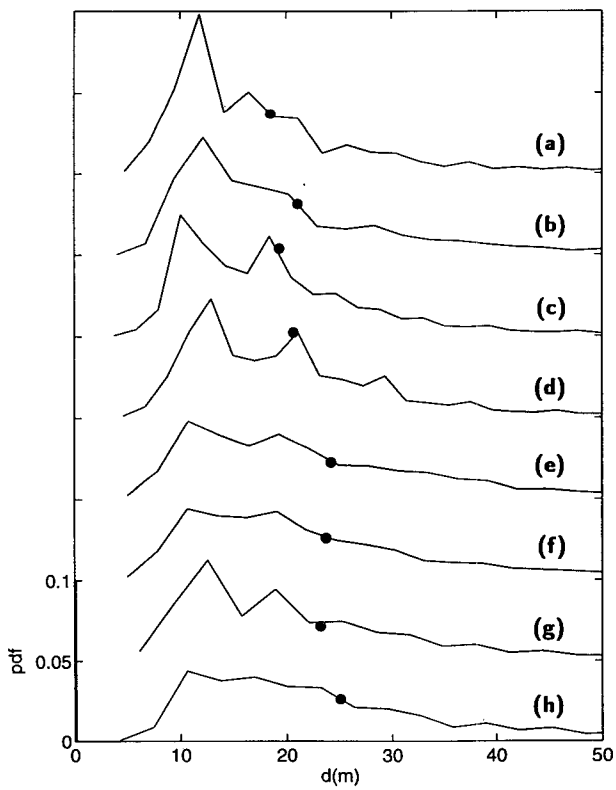

FIG. 12. Probability density function of convergence line spacing, displaced successively by 0.001. Black dots represent the mean spacing. Same time segments as in Fig. 11.

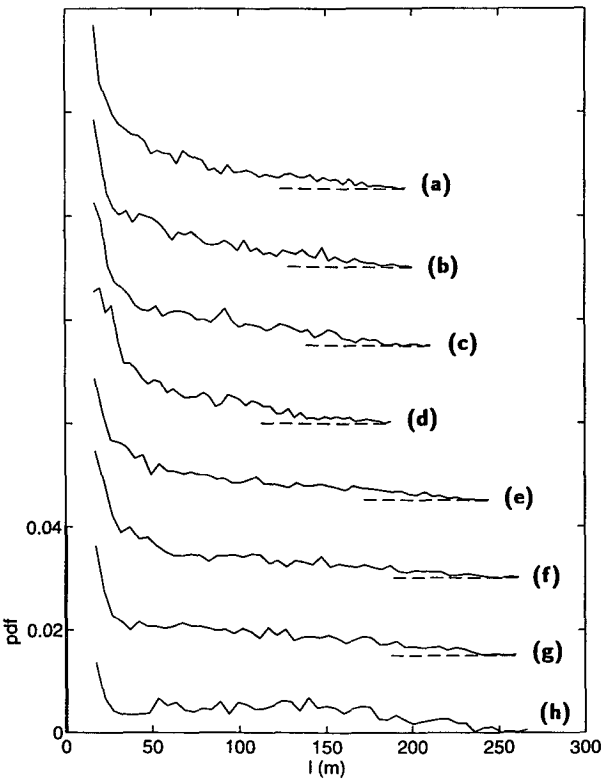

FIG. 13. Probability density function of convergence line length with cutoff at 15 m, displaced successively by 0.012. Same time segments as in Fig. 11.

nant wavelength, or about 12 m, consistent with our prior interpretation of Fig. 10c. Based on these distributions we will not include the shorter bubble clouds in our evaluation of bubble cloud properties.

Although the number of short clouds is large, they only contribute approximately 18% to the total coverage and are not particularly significant. This result is relevant to the interpretation of bubble clouds probed with a vertical sonar, since it implies that only a relatively small fraction of the observed features are directly related to wave breaking events.

Figure 10b presents a histogram of spacing between neighboring convergence lines for the same half period. Lines shorter than 15 m are deleted. Unlike length and direction for which the data are scarce, the spacing has been well studied with the conclusion that Langmuir cells have multiple sizes (e.g., Zedel and Farmer 1991). Our observations confirm this view; spacings between 5 and 50 m were observed. The mean spacing is at d_m = 18.3 m with a standard deviation of σ_d = 10.7 m. The large ratio of σ_d/d_m reinforces the notion of disparity of windrow spacing, as do the skewness $S_d = 2.3$ and kurtosis $F_d = 11.4$. Thus, the spacing distribution is skewed and significantly peaked, compared to a normal distribution ($S_d = 0$, $F_d = 3$). From these results we infer that Langmuir cells, although encompassing various sizes, have a dominant spacing, possibly determined by external forcing such as the wind speed and the depth of the mixed layer.

In the next three diagrams, Figs. 11–13, we examine the temporal evolution of direction, spacing, and length of convergence lines. The times of datasets a, b, c, etc. in these figures are shown on the wind speed time series (Fig. 3). The mean direction falls within 20° of the wind direction (Fig. 11). The standard deviation (~16°) does not change significantly with time, and there appears to be a slight bias in orientation toward the right. As expected, the wind direction determines the orientation of Langmuir convergence lines. Figure 12 shows that the spacing distribution has a mean that appears to increase slightly with increasing wind speed. As discussed above, short bubble clouds (<15 m) are likely associated with breaking waves and are not included in the distributions of convergence line length (Fig. 13). Comparing these histograms, it is apparent that the longer lines occupy a larger proportion of the surface as wind speed increases. Moreover, the longest lines grow with time. Thus, there is a general trend for convergence lines to lengthen with wind speed.

Convergence lines are only apparent in our images where bubbles are present. A referee has questioned whether the statistics of line lengths, for example, could be affected by the intermittent nature of the bubble source (i.e., breaking waves). While a detailed calculation of the stochastic distribution of bubbles is beyond the scope of this paper, we can make an estimate of this effect from the following information: the observed mean spacing between convergence zones is 20 m, a mean transverse velocity of 0.05 m s^{-1} can be estimated from neutrally buoyant float tracks acquired during the storm (E. D'Asaro 1994/3, personal communication), and the frequency of wave breaking was observed to be 0.02 s^{-1} (Farmer et al. 1993). With the mean location of breaking waves chosen to be at half the distance between the convergence and divergence zones, the mean advection time from the breaking wave to convergence zone is of order 100 s. Bubble lifetimes can depend in a complex way on several factors, but for our 100-kHz sonars with resonant bubble radius 32 μm and bubble rise speed of 0.0035 m s^{-1}, a lifetime of order 570 s is implied for an initial penetration depth of 2 m. By comparison, bubbles in a ship wake have been observed to last approximately 9 min (Trevorrow et al. 1994). Thus, a breaking wave frequency of 0.02 s^{-1} should replenish the convergence zone before the previous bubbles have disappeared. This calculation does not rule out the possibility of bubble gaps but it does suggest that it will not be a major factor at these wind speeds. Moreover, it should also be noted that those bubbles that reach the convergence line are subject to shear dispersion, which spreads them out along the downwelling zone, thus reducing the likelihood of an unmarked portion.

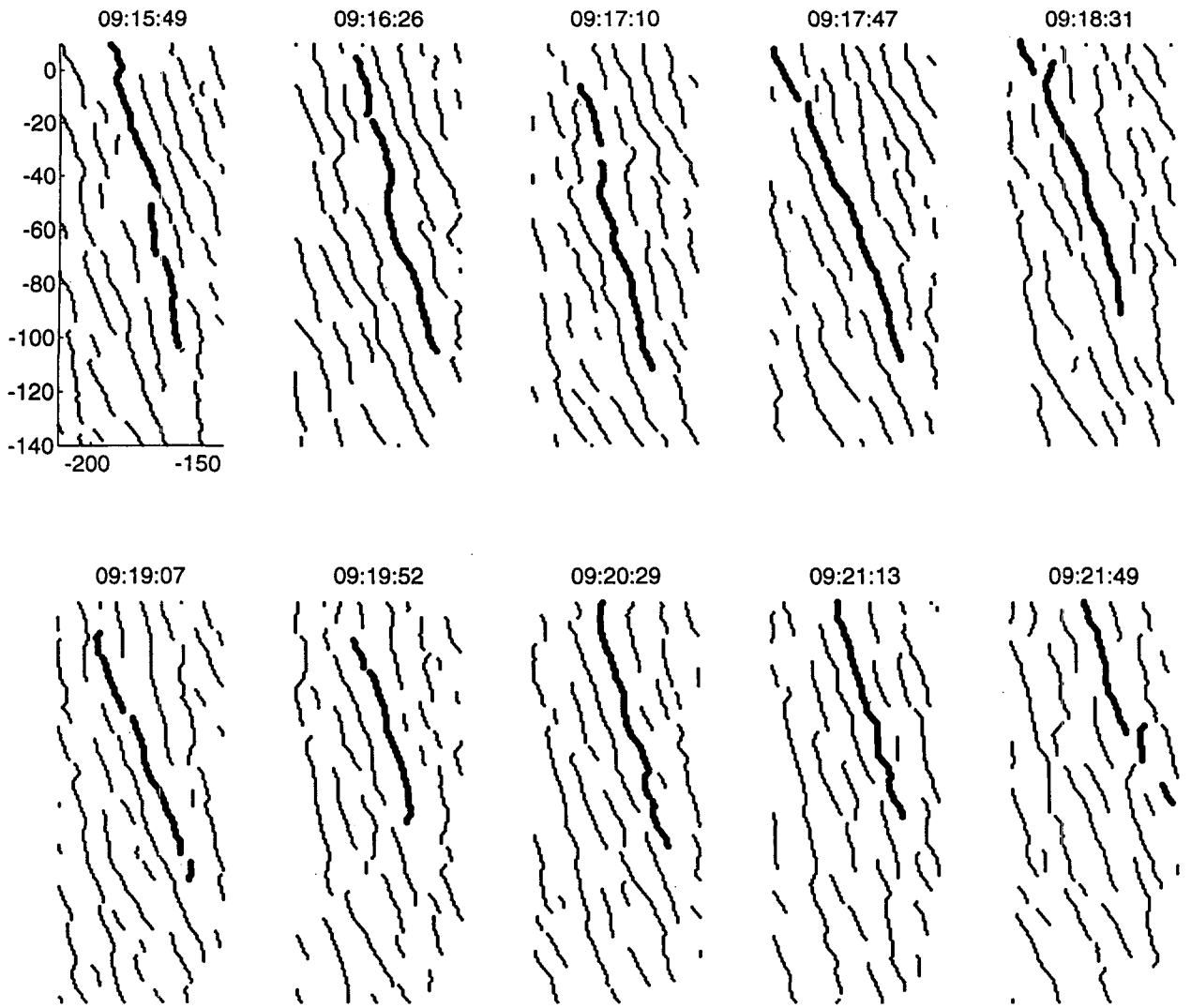

FIG. 14. Successive convergence line patterns for the location selected in Fig. 9 during a rising wind spanning a period of 6 minutes. A single line, shown in bold, has been identified by using overlays of successive images.

Figure 14 illustrates the persistence and time evolution of convergence lines lying within the rectangular area framed in Fig. 9. Unambiguous identification of the convergence lines in successive images is readily achieved using image overlays. A simple overlay of two successive images shows considerable similarity, with convergence lines clearly identifiable over several images. By tracking a single line through adjacent images, both backward and forward in time, it is possible to observe the temporal evolution of individual features. As shown in Fig. 14, where the convergence line (shown in bold) identified at 0818:31 is tracked in this way backward and forward through a total of 10 images. However, there are significant local changes to the structure. These arise both from distortion over scales of tens of meters and from structural changes such as break up and merging. Moreover, small structures ($\leq$15 m) do not generally persist from one image to the next.

5. Y junctions

When the wind speed reached about 13 m s^{-1} at 1000, the surface pattern of bubble clouds lost the regular linear structure apparent at lower wind speeds. Nonparallel and intersecting lines appeared. A dominant pattern occurs in which three linear bands of bubble clouds join together to form a Y shape. In Fig. 7 we saw two such junctions located close to the bottom boundary of the image and one near the top corner. These Y junctions are apparently oriented in the same direction, pointing downwind.

The three lines that form a Y junction converge but do not actually join up at the center point. Analysis of

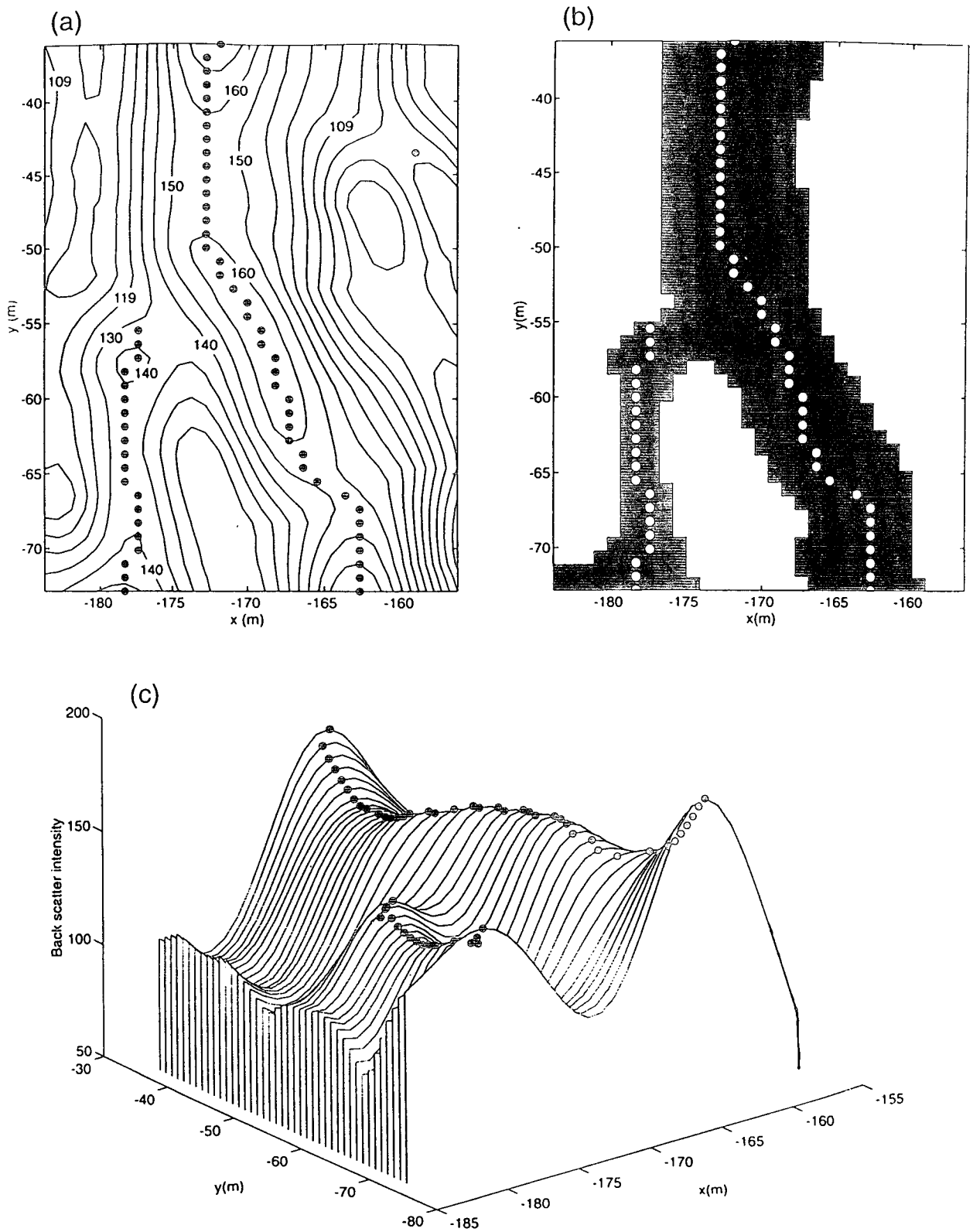

FIG. 15. (a) Contours of smoothed sonar backscatter intensity near a Y junction together with the points identified by the maxima detection method. (b) Junction of the two ridges detected by the threshold method, together with convergence points (shown in white) identified by the maxima detection method. (c) The 3D distribution of filtered sonar intensity showing ridge bifurcation.

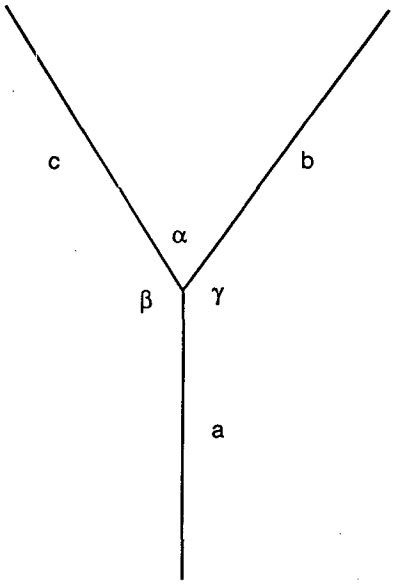

FIG. 16. Schematic diagram of a Y junction.

the raw data shows that the bubble clouds are continuous, but as discussed above they are not connected in our binary representation due to the filtering procedure. The Y junction is shown in more detail in the contour map of the sonar backscatter intensity in Fig. 15a. Convergence points are located at the peak values of the sonar backscatter intensity, although the intensity varies along the two convergence lines. The variability is better illustrated in a three-dimensional diagram (Fig. 15c). We observe a dominant ridge roughly parallel to the y axis, bifurcating into a second lower ridge at $y = -50$ m. The black dots on top of the intensity surface represent the convergence points. Although the trend suggests that the two lines join up, they are separated by the filter cutoff distance.

To overcome this limitation, we add a third step to our algorithm. We set a threshold of backscatter intensity below which all data are discarded and use the resulting pattern to determine the presence or absence of a junction. Figure 15b illustrates the convergence zones mapped by this threshold technique. A Y junction is detected and the two lines are therefore joined. The choice of threshold level is made so as to provide patterns that are consistent with the overall structure of line representations previously derived. The use of a threshold detection at this step of our algorithm is similar to the first stage of Thorpe and Cure's (1994) skeletonizing technique.

The density of Y junctions increases greatly with wind speed. These junctions have a unique geometry and orientation. For convenience in the following discussion, Fig. 16 shows a schematic diagram of a Y junction. The length of the trunk is denoted by a, the right branch by b, and left branch by c. The angles formed between two branches are α, β, and γ, respectively.

Figure 17 shows histograms for the three lengths of Y junctions observed in a half-hour period. A total of 85 Y junctions were detected. The mean values of the

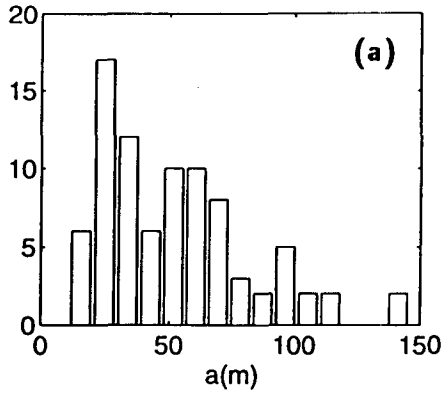

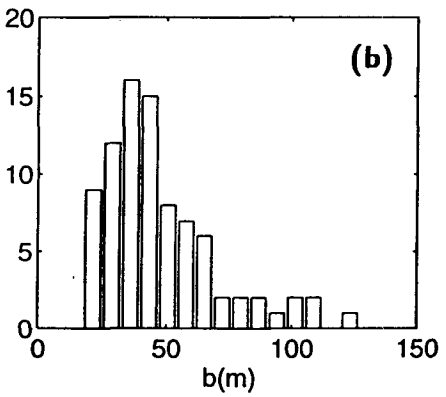

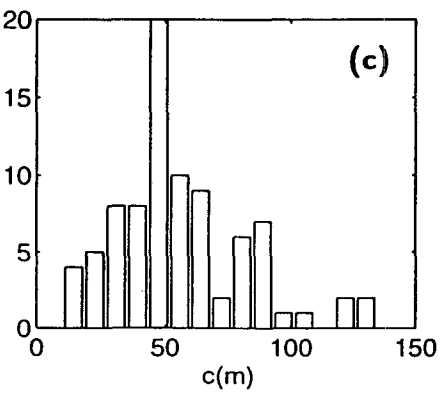

FIG. 17. Measured distribution of 85 Y junctions during the period 1018 and 1050 h. The mean values of three lengths are $a_m = 48.0$ m, $b_m = 52.4$ m, and $c_m = 54.2$ m.

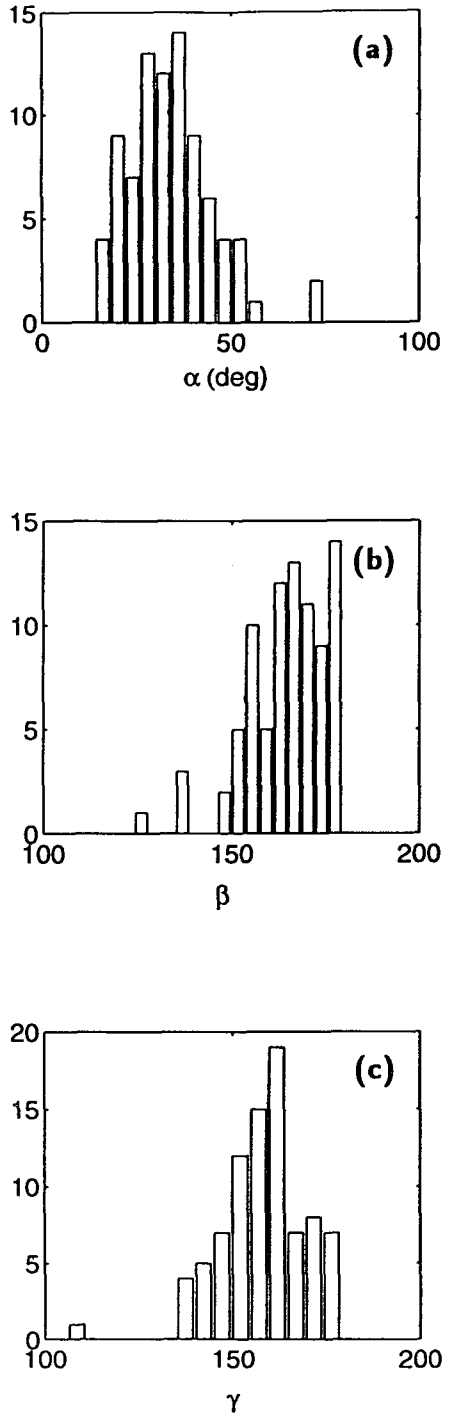

FIG. 18. Y junction angle distribution. The mean values are α = 34.9°, β = 164.9°, and γ = 158.8°. The standard deviation is about 11° for all three angles.

branch lengths are a_m = 52.4 m, b_m = 47.8 m, and c_m = 56.4 m, with a standard deviation between 20 and 30 m. It thus appears that the three branches of a Y junction are of approximately equal length, roughly three times the average spacing between convergence lines.

The corresponding distribution of angles between the three intersecting convergence lines are shown in Fig. 18. The mean value of α is about 35°, and $\beta \approx \gamma \approx 162°$. The standard deviation of the angle measurements is around 11°. Measurements of α in other datasets give a mean value of 30° with little variability.

Most Y junctions point downwind (Fig. 19). A few point upwind, but they do not survive through two successive images and were excluded in the statistics.

Y junctions can be tracked in a sequence of images, as shown in Fig. 20. The Y junction appears in all images spanning a period of 6 minutes. It is interesting to note that other lines join the primary structure to form a treelike structure in later images. Figure 21 shows a two-dimensional correlation of two successive images in this data. Although there is a well-defined maximum, the correlation of 0.5 is lower than might be expected based on a visual comparison of images. This is partly due to the fact that rotation is not a free parameter and partly to variability in the smaller-scale structure.

6. Discussion

Bubbles are tracers of the flow field. When bubbles organize into long and parallel lines, they indicate that Langmuir vortices are counterrotating longitudinal vortex tubes. On the other hand, Y-junction patterns of bubble clouds suggest the formation of U-shaped vortices as a result of vortex reconnection (see Fig. 22).

Crow (1970) examined the three-dimensional instability of a counterrotating vortex pair and found

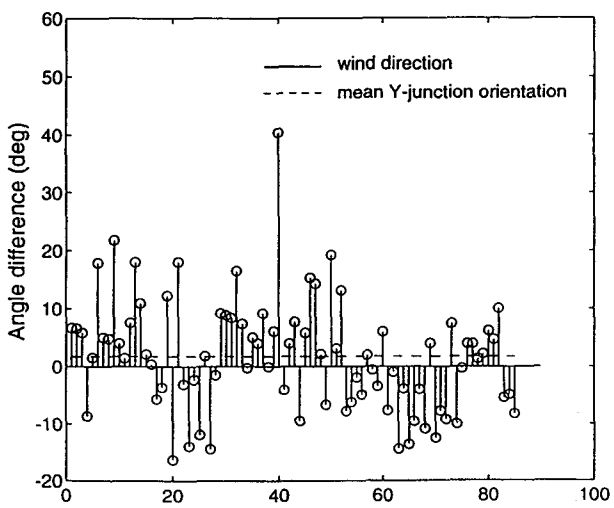

FIG. 19. Angular deviation of Y junctions with respect to the wind direction. Angle difference is positive when the trunk of a Y junction lies to the left of the downwind direction and negative when the trunk lies to the right.

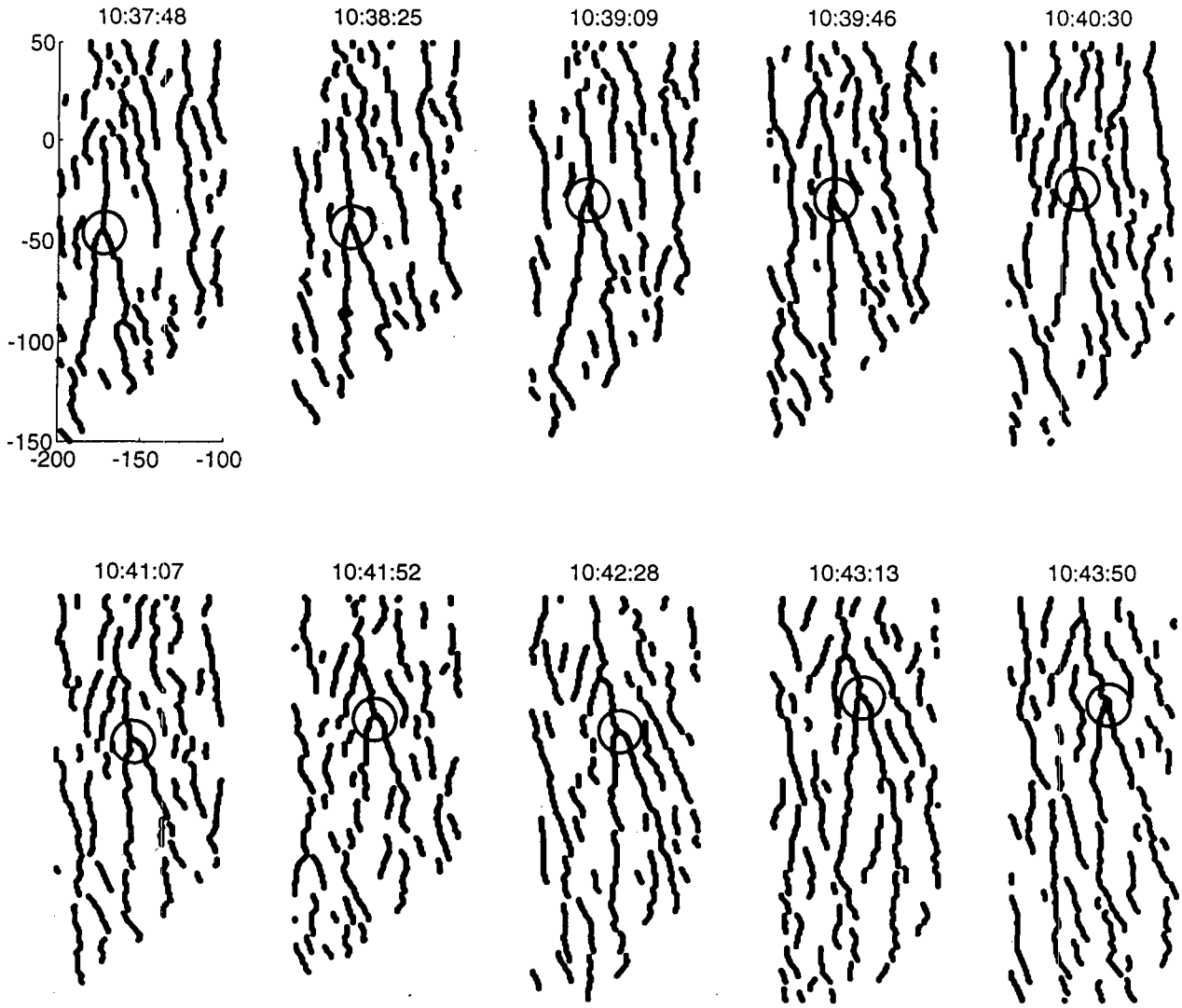

FIG. 20. Evolution of a Y junction over a 6-minute period.

that a wavelike disturbance may grow. Eventually the two vortices touch each other at certain points (Moore 1972). This results in breaking and rejoining of the vortices. The key mechanism in the vortex reconnection is that viscosity cancels the vorticity where the filaments first touch, so that the vortices will be cut off. The rejoining is not seen as a separate process but as a consequence of the kinematic theorem that vortex lines cannot end inside a fluid (Saffman 1990). Shelley et al. (1993) have numerically simulated this process of vortex reconnection.

We propose that reconnection of counterrotating vortex tubes is responsible for the formation of Y-junction convergence zones. A schematic diagram illustrating the convergence lines and the underlying vortex structure is shown in Fig. 22. Parallel vortex filaments are subject to the vacillating mode of instability, as discussed by Thorpe (1992b). Further growth of the instability leads to the cutoff and subsequent rejoining of the two vortex tubes. This results in the formation of two U-shaped vortices. The convergence zones between the U-shaped vortices and two adjacent parallel vortices form a Y junction and an inverted Y junction.

Most of the Y junctions point downwind. However, both downwind Y junctions and inverted Y junctions are permitted by the analysis of vortex motion.

What is missing in the vortex model that might account for the preferred orientation of Y junctions? The dominant source of vorticity in the ocean surface layer derives from the wind-driven shear current. The vorticity associated with this shear is oriented crosswind and always to the left of the wind direction. This crosswind vorticity reinforces the vorticity at the tip of the U-vortex tube pointing downwind but offsets the vorticity at the tip of the U-vortex tube pointing in the

opposite direction (see Fig. 22c). As a result of the opposing wind driven vorticity, the U-vortex pointing upwind can be expected to decrease in intensity, and so the inverted Y junction may be destroyed. In this way the crosswind vorticity associated with the mean shear determines the predominant orientation of the Y junctions.

7. Conclusions

Using a two-dimensional imaging sonar technique, we have observed the spatial patterns of bubble clouds at the sea surface. It is found that three linear bands of bubble clouds join together to form a Y shape. Statistical analysis of sonar images shows that Y junctions have a unique geometry and orientation. Understanding of this pattern requires an extension of the two-dimensional Craik–Leibovich (1976) model, and the observations described here have motivated a separate study using a three-dimensional model to analyse the vortex interaction. Preliminary calculations suggest that the acute angle of convergence line intersections depends on the development of the Crow instability, which has a preferred wavelength much greater than the spacing between the vortices.

For the Kelvin–Helmholtz instability, the effects of "junctions" between neighboring vortices on momentum and density transfer might be comparable to that associated with the smaller scale transfers associated with the two-dimensional rollup into billows (Thorpe 1994/3, personal communication). Although our observations are limited to a single storm (12 h), it appears that during the period of measurement the three dimensionality of these structures is an essential feature of Langmuir circulations at higher wind speeds.

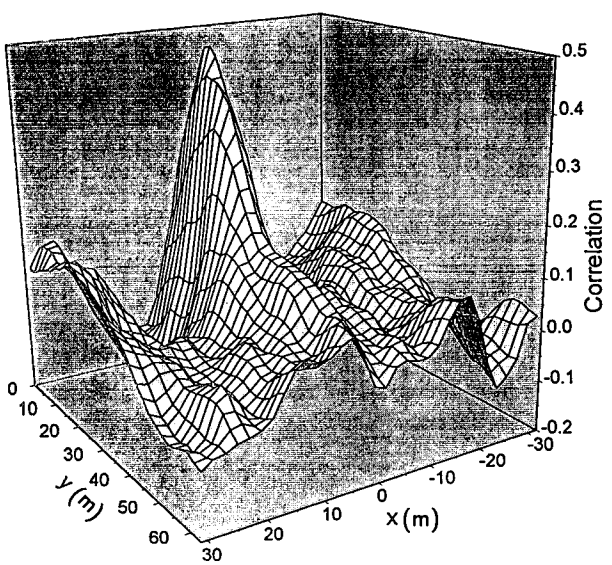

FIG. 21. A two-dimensional correlation function obtained by cross-correlating two successive raw backscatter images. The correlation does not allow for rotation.

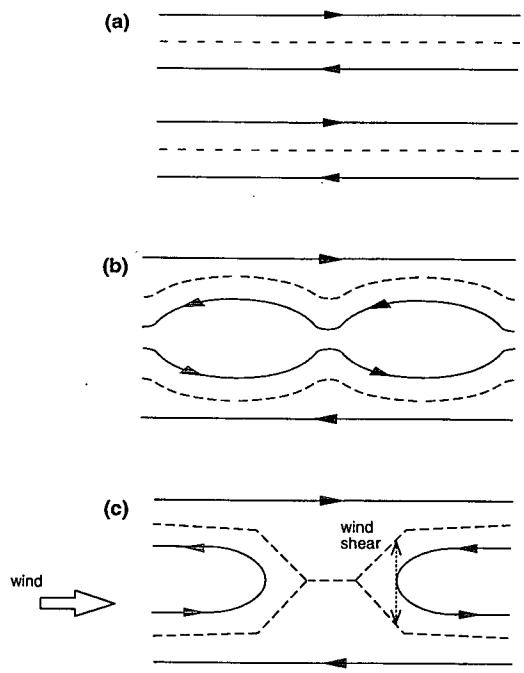

FIG. 22. A schematic diagram showing the vortex reconnection process and formation of U-shaped vortex tubes. Solid lines represent lines vortices with arrows indicating the signs of circulation, while dashed lines represent convergence zones. (a) Parallel vortex lines, (b) vacillating mode of instability, and (c) U-shaped vortices formed after vortex reconnection. The convergence lines between the vortex tubes form a Y junction and an inverted Y junction.

Acknowledgments. Chris Garrett and Mark Trevorrow contributed to valuable discussions during the course of this work; Xiaohong Wang, Donald Booth, and Richard Outerbridge assisted with the development of the line detection schemes. Victor Yixin Mao assisted in the data analysis and Rosalie Rutka helped prepare the diagrams. This work is supported by the U.S. Office of Naval Research and Canadian Panel on Energy Research and Development, Project No. 67189.

REFERENCES

Craik, A. D. D., and S. Leibovich, 1976: A rational model for Langmuir circulations. *J. Fluid Mech.*, **73**, 401–426.

Crow, S. C. 1970: Stability theory for a pair of trailing vortices. *A.I.A.A.J.*, **8**, 2172–2179.

Ding, L., and D. M. Farmer, 1994: Observations of breaking surface wave statistics. *J. Phys. Oceanogr.*, **24**, 1368–1387.

Etling, D., and R. A. Brown, 1993: Roll vortices in the planetary boundary layer: A review. *Bound. Lay. Meteor.*, **65**, 215–248.

Farmer, D. M., C. McNeil, and B. Johnson, 1993: Evidence for the importance of bubbles to the enhancement of air–sea gas flux. *Nature*, **361**, 620–623.

Guo, Y., and W. H. Finlay, 1994: Wavenumber selection and irregularity of spatially developing nonlinear Dean and Gortler vortices. *J. Fluid Mech.*, **264**, 1–40.

Langmuir, I., 1938: Surface motion of water induced by wind. *Science,* **87,** 119–123.

Leibovich, S., 1983: The form and dynamics of Langmuir circulation. *Annu. Rev. Fluid Mech.,* **15,** 391–427.

Moore, D. W., 1972: Finite amplitude waves on aircraft trialing vortices. *Aero. Quart.,* **23,** 307–314.

Newell, A. C., T. Passot, and M. Souli, 1990: The phase diffusion and mean drift equations for convection at finite Rayleigh numbers in large containers. *J. Fluid Mech.,* **220,** 187–252.

——, ——, and J. Lega, 1993: Order parameter equations for patterns. *Annu. Rev. Fluid Mech.,* **25,** 399–453.

Osborn, T., D. M. Farmer, S. Vagle, S. A. Thorpe, and M. Cure, 1992: Measurements of bubble plumes and turbulence from a submarine. *Atmos.-Ocean,* **30**(3), 419–440.

Pierrehumbert, R. T., and S. E. Widnall, 1982: The two- and three-dimensional instabilities of a spatially periodic shear layer. *J. Fluid Mech.,* **114,** 59–82.

Saffman, P. G., 1990: A model of vortex reconnection. *J. Fluid Mech.,* **212,** 395–402.

Shelley, M. J., D. I. Meiron, and S. A. Orszag, 1993: Dynamical aspects of vortex reconnection of perturbed anti-parallel vortex tubes. *J. Fluid Mech.,* **246,** 613–652.

Smith, J. R., R. Pinkel, and R. Weller, 1987: Velocity structure in the mixed layer during MILDEX. *J. Phys. Oceanogr.,* **17,** 425–439.

Thorpe, S. A., 1992a: Bubble clouds and the dynamics of the upper ocean. *Quart. J. Meteor. Soc.,* **118,** 1–22.

——, 1992b: The break-up of Langmuir circulation and the instability of an array of vortices. *J. Phys. Oceanogr.,* **22,** 350–360.

——, 1985: Laboratory observations of secondary structures in Kelvin–Helmholtz billows and consequences for ocean mixing. *Geophys. Astrophys. Fluid Dyn.,* **34,** 175–199.

——, and A. J. Hall, 1983: The characteristics of breaking waves, bubble clouds, and near surface currents observed using side-scan sonar. *Contin. Shelf Res.,* **1,** 353–384.

——, and M. S. Cure, 1994: One-dimensional dispersion in a lake inferred from sonar observations. *Mixing and Transport in the Environment,* K. J. Bevan, P. C. Chatwin, and J. H. Millbank, Eds. Wileys Publications, 17–28.

Trevorrow, M. V., S. Vagle, and D. M. Farmer, 1994: Acoustical measurements of micro bubbles within ship wakes. *J. Acoust. Soc. Amer.,* **95**(4), 1922–1930.

Vagle, S., and D. M. Farmer, 1992: The measurement of bubble size distributions by acoustical backscatter. *J. Atmos. Oceanic Technol.,* **49,** 630–644.

Weller, R. A., and J. F. Price, 1988: Langmuir circulation within the oceanic mixed layer. *Deep-Sea Res.* **35,** 711–747.

Zedel, L., and D. Farmer, 1991: Organized structures in subsurface bubble clouds: Langmuir circulation in the open ocean. *J. Geophys. Res.,* **96,** 8889–8900.